

Soft Matter

Accepted Manuscript



This is an *Accepted Manuscript*, which has been through the Royal Society of Chemistry peer review process and has been accepted for publication.

Accepted Manuscripts are published online shortly after acceptance, before technical editing, formatting and proof reading. Using this free service, authors can make their results available to the community, in citable form, before we publish the edited article. We will replace this *Accepted Manuscript* with the edited and formatted *Advance Article* as soon as it is available.

You can find more information about *Accepted Manuscripts* in the [Information for Authors](#).

Please note that technical editing may introduce minor changes to the text and/or graphics, which may alter content. The journal's standard [Terms & Conditions](#) and the [Ethical guidelines](#) still apply. In no event shall the Royal Society of Chemistry be held responsible for any errors or omissions in this *Accepted Manuscript* or any consequences arising from the use of any information it contains.

Bubble-Surface Interactions with Graphite in the Presence of Adsorbed Carboxymethylcellulose

Jueying Wu^{1,2}, Iliana Delcheva¹, Yung Ngotha², Marta Krasowska^{1}, David A. Beattie^{1*}*

¹Ian Wark Research Institute, University of South Australia, Mawson Lakes SA 5095, Australia.

²School of Chemical Engineering, University of Adelaide, Adelaide SA 5005, Australia;

* Corresponding Authors: E-mail: Marta.Krasowska@unisa.edu.au, Telephone number: +61 8 8302 6861 (Marta Krasowska); E-mail: David.Beattie@unisa.edu.au, Telephone number: +61 8 8302 3676 (David A. Beattie).

ABSTRACT

The adsorption of carboxymethylcellulose (CMC), and the subsequent effect on bubble-surface interactions, has been studied for a graphite surface. CMC adsorbs on highly oriented pyrolytic graphite (HOPG) in specific patterns: when adsorbed from a solution of low concentration it forms stretched, isolated and sparsely distributed chains, while upon adsorption from a solution of higher concentration, it forms an interconnected network of multilayer features. The amount and topography of the adsorbed CMC affect the electrical properties as well as the wettability of the polymer-modified HOPG surface. Adsorption of CMC onto the HOPG surface causes the zeta potential to be more negative and the modified surface becomes more hydrophilic. This increase in both the absolute value of zeta potential and the surface hydrophilicity originates from the carboxymethyl groups of the CMC polymer. The effect of the adsorbed polymer layer on wetting film drainage and bubble-surface/particle attachment was determined using high speed video microscopy to monitor single bubble-surface collision, and single bubble Hallimond tube flotation experiments. The time of wetting film drainage and the time of three-phase contact line spreading gets significantly longer for polymer-modified HOPG surfaces, indicating that the film rupture and three-phase contact line expansion were inhibited by the presence of polymer. The effect of longer drainage times and slower dewetting correlated with reduced flotation recovery. The molecular kinetic model was used to quantify the effect of the polymer on dewetting dynamics, and showed an increase in the jump frequency for the polymer adsorbed at the higher concentration.

INTRODUCTION

The interaction of bubbles with solid surfaces is simultaneously a fertile ground for fundamental studies of hydrodynamics¹⁻³, wetting/dewetting⁴⁻⁷, and surface forces in soft matter^{1-3, 8-10}, and one of the most widespread and important colloidal process in the mineral processing industry. Froth flotation is the dominant process for the separation and concentration of base metals from metal sulfide ores¹¹. Flotation involves the suspension of finely ground mineral particles in an aqueous mixture of chemicals (termed a mineral slurry, feed, or pulp), and the passage of air bubbles through the mixture. Particles of high hydrophobicity, i.e. low surface energy, attach to air bubbles and rise to the surface of the flotation vessel. Particles of low hydrophobicity are unable to attach to air bubbles and thus remain in the mineral mixture. The interaction of bubbles with solid particles is central to this process^{12, 13}, and to fully understand and optimise mineral recovery, one needs to understand the fundamentals of bubble-surface/particle collisions^{6, 7, 14}, and the influence of adsorbed chemicals on bubble-surface attachment^{15, 16}.

The chemicals used in the slurry are deployed to ensure that valuable minerals are hydrophobic (and thus attach to air bubbles), and to ensure that worthless minerals (termed gangue) are prevented from attaching to air bubbles¹⁷. This latter objective is classified as mineral depression, and is achieved by altering the surface properties of the gangue – either by chemical reactions (e.g. oxidation) to reduce the surface hydrophobicity, or by adsorption of organic polymers that interrupt the bubble-particle attachment process¹⁷. The chemicals used for this purpose are termed depressants. The action of a depressant is determined by the nature of the chemical itself. Inorganic depressants act primarily by reacting with the surface and reducing the innate hydrophobicity of the mineral (such as the action of sulphite ions on pyrite and sphalerite^{18, 19}). Organic polymers act by adsorption, and their action as depressants was theorised to be due to increasing the time it takes for the bubble to connect to

a mineral particle (termed drainage and wetting film rupture time), slowing down the speed with which the bubble spreads over the particle (the rate of dewetting or time of the three-phase contact spreading), and by reducing the overall hydrophobicity of the particle^{20, 21}.

This multiple-mode action of polymer depressants was recently confirmed experimentally by a series of studies from this group²²⁻²⁵. The importance of wetting film rupture time and prolonged dewetting of mineral surfaces in the flotation of minerals was demonstrated for talc (a problematic gangue mineral) and for molybdenite (an exceptionally valuable metal sulfide mineral). In this current study, we have focused on graphite as the mineral of interest, and the effect of adsorbed polymers on the attachment of bubbles to a graphite surface. Graphite particles have a planar structure, with large areas of exposed non-polar hydrophobic surface. The dominance of the hydrophobic surface (termed the basal plane) on graphite particles is exploited in the mineral processing of graphite deposits – with flotation being used to concentrate and separate the graphite from the other ore components^{26, 27}. In other ore deposits, the presence of graphite or graphitic material causes problems in the concentration of other minerals²⁸⁻³⁰, and thus particles with graphitic surfaces need to be depressed.

Our approach for this investigation has involved detailed studies of bubble-surface collisions, using high speed video microscopy. This has enabled a comprehensive investigation of wetting film rupture and dynamic dewetting for bare graphite, and for graphite exposed to varying solution concentrations of carboxymethylcellulose (CMC), a commonly studied flotation depressant³¹⁻³⁴. The influence of CMC on the bubble-surface attachment process for graphite is discussed in the context of the adsorbed layer morphology of CMC on graphite, as determined using atomic force microscopy imaging. Dynamic dewetting, and the role of CMC in prolonging the process, is further examined using Molecular Kinetic (MK) model. Finally, the results obtained for model (HOPG-bubble)

system were compared with single bubble Hallimond tube flotation data for graphite particles.

MATERIALS AND METHODS

Solid Surfaces and Solutions Preparation: Two types of graphite surfaces as shown in Figures 1A and 1B were used in this study. Highly ordered pyrolytic graphite (HOPG) flat surfaces with a surface area of $1 \times 1 \text{ cm}^2$ were purchased from SPI Supplies (USA) and were of SPI-1 grade. Such surfaces were used for Atomic Force Microscope (AFM) imaging, bubble collision, and zeta potential determination experiments. For zeta potential determination, the flat surface of HOPG was cut to the size of a disc of diameter of 10 mm. The second type of graphite surfaces were graphite particles (purchased from Aldrich). The Brunauer-Emmett-Teller (BET) surface area³⁵ was measured to be $3.0 \text{ m}^2 \text{ g}^{-1}$ (determined by N_2 adsorption, using a ASAP 2000 BET Analyzer, Micromeritics, USA). The particle size distribution was determined by AccuSizer 770 to be 0.5-29 μm , with a peak particle count (centre of the distribution) at 11 μm . Graphite particles were used for single bubble Hallimond tube flotation experiments.

KCl (99%, AR) was purchased from Chem-Supply, Australia. KCl was then calcined at 550 °C for 8 hours to remove any organic impurities, recrystallised, and then again calcined at 550 °C for another 8 hours. The purified KCl was then transferred to a clean glass bottle with a glass stopper and stored in a glass desiccator. 0.001 M KCl solution was prepared using purified KCl and Milli-Q water (supplied by an Advantage A10 system (Millipore, USA)) of a resistivity of $18.2 \text{ M}\Omega \cdot \text{cm}$ and an interfacial tension of $72.4 \text{ mN} \cdot \text{m}^{-1}$ at 22 °C, and a total organic carbon component of less than $4 \text{ mg} \cdot \text{L}^{-1}$. The solution was then heated up to 50 °C for 30 min, and upon its cooling, an ultra-pure dried nitrogen stream (99.999%, BOC, Australia) was bubbled through a glass porous frit into the KCl solution for 45 min. This step

allows for CO₂ removal and thus any pH fluctuations due to CO₂ dissolution are minimised. The pH of 0.001 M KCl was then adjusted to 9 using 0.1 M and 0.01 M KOH (volumetric grade, Scharlau, Spain). The choice of solution pH is determined by the application of mineral flotation, which is characteristically performed under mild alkaline conditions¹¹. The interfacial tension of such background electrolyte solution was 72.4 mN·m⁻¹ at 22 °C.

Sodium carboxymethylcellulose (CMC) was purchased from Sigma-Aldrich and had a molecular weight of 90,000 g·mol⁻¹ and a degree of substitution of 0.7 (for every 10 monomers, 7 have a carboxymethyl substitution). The structure of the polymer is given in Figure 1C. Stock solutions of CMC (at either 2,000 or 5,000 mg·L⁻¹) were prepared in 0.001 M KCl at neutral pH and stirred overnight. The solution was then diluted with 0.001 M KCl at pH 9 prior the experiments. All CMC solutions were prepared and used within 24 h.

CMC Adsorption: In order to ensure that the polymer concentration per surface area of graphite was the same in all the experiments, the solid and particulate graphite samples were exposed to different amounts and concentrations of the CMC solution. For AFM and bubble collision experiments CMC was adsorbed onto a flat and square (1 × 1 cm²) HOPG surface from 10 mL of either 5 or 25 mg·L⁻¹ CMC solution. For zeta potential determination experiments CMC was adsorbed onto a flat and circular (circle diameter 1 cm) surface area from 7.9 mL of either 5 or 25 mg·L⁻¹ CMC solution. For single bubble Hallimond tube flotation 0.003 g of graphite particles were stirred with 100 mL of either 45 or 225 mg·L⁻¹ CMC solution.

The adsorption time was kept constant for all experiments, and was fixed at 30 min. This is sufficient time for CMC to adsorb onto hydrophobic surfaces³⁶. After the adsorption, the square and round flat HOPG surfaces were rinsed with 0.001 M KCl at pH 9 and used for the experiments. The graphite suspensions were transferred to the Hallimond tube after 30 min of

adsorption time, and single bubble flotation was carried out immediately. All experiments were conducted at $22 \pm 1^\circ\text{C}$.

Atomic Force Microscopy Imaging: *In situ* AFM imaging was used to collect topographic information about freshly cleaved (bare) and CMC-modified HOPG surfaces. The AFM (a Nanoscope MultiMode 8 AFM (Bruker, USA) with a Nanoscope V controller (Bruker, USA)) was used in peak force tapping (PFT) mode. PFT AFM is an intermittent contact mode, in which the cantilever is oscillated at a frequency of 2 kHz, much below its resonance frequency. Such a frequency is sufficiently fast for imaging, but also allows one to measure, and thus control, the force profile. Such direct force control helps protect both the tip and sample (even very soft material) from damage, and therefore avoids the acquisition of image artifacts³⁷.

In situ AFM imaging was performed using a commercially available quartz fluid cell in open configuration, i.e. without an O-ring. Prior to the experiment, flat $1 \times 1 \text{ cm}^2$ freshly cleaved or CMC-modified HOPG surfaces were placed on the AFM scanner. A small amount ($\sim 1 \text{ mL}$) of 0.001 M KCl at pH 9 was placed onto the HOPG surface using a clean glass transfer pipette. The quartz fluid cell with a mounted AFM cantilever was placed over the HOPG surface, a meniscus was formed between the HOPG sample and the cell. In order to minimise the effect of solution evaporation and therefore an increase in the ionic strength of the solution during scanning, a small amount of solution ($\sim 150 \mu\text{L}$) was added at 30 min intervals. A piezoelectric scanner E, with a maximum $10 \times 10 \mu\text{m}^2$ scan size in the XY-plane and nominal $2.5 \mu\text{m}$ in the Z direction was used to collect several $500 \times 500 \text{ nm}^2$ and $1 \times 1 \mu\text{m}^2$ images at several positions on the sample. To acquire images silicon nitride cantilevers with a resonance frequency between 40 and 75 kHz, a spring constant between 0.12 and 0.48 $\text{N}\cdot\text{m}^{-1}$, and a sharp silicon (nominal tip radius 2 nm) tip (SCANASYST-FLUID+, Bruker,

USA) were used. All images were taken at high resolution (512×512 pixels), giving a pixel size of 1.9 nm (for $1 \times 1 \mu\text{m}^2$ scans) or 1 nm (for $500 \times 500 \text{ nm}^2$ scans), i.e. comparable to the nominal tip radius. Scan rates employed in imaging were 0.99 Hz or lower. The images were analysed using WSxM 4.0 SPMAGE 09 Edition (Nanotec)³⁸ and NanoScope Analysis v1.5 (Bruker, USA) software packages. In order to remove the image tilt the AFM images were fitted with a first-order plane fit.

Zeta Potential Determination: The zeta potential of freshly cleaved and CMC-modified HOPG surfaces was determined using a ZetaSpin 2.0 instrument (Zetamatrix, USA). The ZetaSpin instrument employs the spinning disc principle³⁹ to measure streaming potential. A freshly cleaved or CMC-modified HOPG disc was mounted onto a sample holder in the ZetaSpin cell filled with 0.001 M KCl at pH 9. A sensing electrode was placed in close proximity (0.5 mm)^a to the central axis of the HOPG surface. The streaming current path goes outward along the disc surface (surface current) and returns through the solution (bulk current) generating a spatially distributed streaming potential⁴¹. The measured streaming potential is the jump in the voltage recorded as the motor switches the sample rotations from off to on, and back off again. The streaming potential was the average taken from 6 independent measurements. The zeta potential, ζ , was determined using the following formula^{b41}:

$$\zeta \cong \frac{1.96\kappa\nu^{1/2}}{\varepsilon a \Omega^{3/2}} \frac{1}{2 \left(1 - \frac{z}{a} - \frac{1}{2 \left(\frac{z^2}{a^2} + 1 \right)^{1/2}} \right)} \phi_s \quad (1)$$

^a Surface conductivity effects at the spinning disc are negligible if the disc radius is larger than the distance from the disc surface to the sensing electrode³⁹

^b Equation (1) is accurate to 1% when z is no more than 10% of the disc radius, $a/2$, which means for the sample of $a = 10 \text{ mm}$, z should not be larger than 0.5 mm.

where: κ is the liquid conductivity, ν is the kinematic viscosity, ε is the liquid permittivity, a is the disc (sample) diameter, Ω is the sample rotation rate (in $\text{rad}\cdot\text{s}^{-1}$), z is the distance between the sample and the reference electrode and ϕ_s is the streaming potential. Measurements were made in triplicate for all conditions.

Bubble-Surface Collisions and Receding Contact Angle Measurements: Bubble-surface collisions and the evolution of the dynamic receding contact angle on freshly cleaved and CMC-modified HOPG surfaces were studied using a rising microbubble apparatus²⁴. The experimental set-up consisted of a borosilicate glass column (of a square cross section of $30 \times 30 \text{ mm}^2$) mounted onto a Teflon column holder with a Pyrex glass microfluidic chip at the bottom for controlled microbubble release. Air bubbles were generated at the T-junction of the microfluidic chip. The flow rates of air and background electrolyte solution (and thus the size and frequency of generated bubbles) were controlled via a precision syringe pump (Cole-Parmer, USA) connected to the microfluidic chip.

The glass column was filled with 0.001 M KCl solution at pH 9. A single air bubble was released every 30-60 s from the microfluidic chip and allowed to rise freely. A freshly cleaved or CMC-modified HOPG surface was located beneath the solution surface, at $\sim 8 \text{ cm}$ above the point of the bubble generation, ensuring bubbles were rising with their terminal velocity. The bubble rise and the collision with the solution-HOPG interface were monitored from the side and recorded by a stereo-microscope (SZ-1145TR, Olympus, Japan) mounted to a high speed video camera (SA3, Photron, USA) at the frequency of 1000 Hz.

To avoid bubble deformation and kinetic effects, such as the bubble bouncing off the solution-solid interface, the bubble collision experiments were carried out using bubbles in

the size range 414 – 448 μm^c . The Weber numbers, We , are between $1.2 \cdot 10^{-2}$ and $1.9 \cdot 10^{-2}$, which ensures that such bubbles maintained a fairly spherical shape during rise and collision⁴³. The Reynolds numbers, Re , for such bubbles are between 22 and 28. The terminal velocities of rising bubbles were measured from the difference in the bubble position as a function of time. The terminal velocities were $47.2 - 55.8 \text{ mm} \cdot \text{s}^{-1}$ for bubbles in the size range 414 – 448 μm . Such experimentally measured values are in a good agreement with the ones predicted by Klaseboer *et al.* for bubbles of $0 < Re < 500$ ⁴⁴. This indicates that the bubble surface is fully mobile and there are no adsorbing surface active impurities in our system⁴⁵.

Upon bubble collision with the solution-HOPG interface, the liquid between the HOPG and the top pole of the bubble starts to drain, forming a thin liquid film. This so-called wetting film drains until a certain thickness and then, depending on the interaction forces acting across the film, either ruptures (if the sum of the interaction forces is attractive) allowing the bubble to attach to and dewet the solid surface, or stays in the form of a stable wetting film (if the sum of the interaction forces is repulsive), preventing bubble attachment. In all the cases discussed in this work, the wetting film was unstable and ruptured. The three-phase contact line (TPCL) expanded after rupture, dewetting the HOPG surfaces. The receding dynamic contact angle, θ_{rec} , was monitored during the dewetting process, until the receding contact angle reached its static value, i.e. no further changes were observed. For all conditions, a minimum of 30 collisions (and a maximum of 50) were observed and recorded.

The sequences of recorded images were further analysed using Photron Motion Tools (for the determination of the bubble diameter, bubble terminal velocity and drainage time), and SCA-202 v 4.3.18 (to measure the receding contact angle and the diameter of the TPCL perimeter as a function of time).

^c Bubbles of diameter $\sim 400 \mu\text{m}$ were shown to have the highest collision efficiency for single bubble Hallimond tube flotation experiments⁴⁷.

The dynamic receding contact angle data was analysed using the molecular kinetic (MK) model. The MK model ⁴⁶ (based on the activated rate theory of Henry Eyring ⁴⁷) postulates that at equilibrium, thermally activated displacements of molecules take place at the contact line, jumping between substrate adsorption sites with an average displacement length of λ_{MK} and a frequency of k_0 at n_{sites} number of sites. When the equilibrium is disturbed, the out-of-balance interfacial tension acts as a driving force to move the contact line in a given direction with a velocity V , given by⁴⁶:

$$V(\Theta) = 2k_0\lambda_{MK} \sinh \left[\frac{\gamma}{2n_{sites}k_B T} (\cos \theta_e - \cos \theta_d) \right] \quad (2)$$

where γ is the liquid-vapor interfacial tension, θ_e and θ_d are the equilibrium and dynamic contact angle^d, respectively, k_B is the Boltzmann constant, and T (295 Kelvin in this study) is the absolute temperature.

The freely available software program, G-Dyna,^{48, 49} was used to fit the receding contact angle versus wetting radius data (determined from the SCA-202 software, and with an estimate of the error in the determined values of $\pm 0.5^\circ$ for receding contact angle; $\pm 5 \mu\text{m}$ for the measured wetting radius). The first stage of the data treatment involved a calculation of the contact line velocity for each contact angle data point (and the determination of the error in the contact line velocity). The second stage of the data treatment was the fitting of the receding contact angle versus contact line velocity data to the general MK model expression (given in (2)), to determine the MK model parameters λ_{MK} and k_0 . To ensure that the MK Model fitting produces statistically sound mean values and standard deviations for the model parameters, the fitting procedure involved 1000 fits to individual datasets generated from one initial input dataset. These 1000 generated datasets were based on the dataset to be fitted, altered in a statistically random manner whereby 37% ($1/e$) of the datapoints are altered to a

^d θ_e is a fitting parameter in MKT and it should be noted that, for non-ideal systems (such as the systems studied in this Manuscript), the 'equilibrium contact angle' is never achieved. θ_d in Equation (2) is dynamic contact angle, and it corresponds to experimentally measured receding dynamic contact angle in this study.

different value, albeit within the error bounds of the initial data points. This dataset generation was performed using a bootstrap numerical technique.

Single Bubble Flotation: The experiments were conducted in a modified Hallimond tube⁵⁰ shown in Figure 2. The flotation tube consists of a bottom and top borosilicate columns (bottom column has a square cross-section of $20 \times 20 \text{ mm}^2$, while the upper one has a circular cross-section of a diameter of 12 mm). Both columns are joined via a three-way valve. The bottom column is filled with the particle suspension while the top one – with background electrolyte – produces a particle-free zone prior the collection of the concentrate. Such a design helps to reduce entrainment (collection of particles without bubble attachment – i.e. carried along with a stream of bubbles by liquid flow).

The experiments were performed as follows. The three-way valve was turned to the position ‘A’ (Figure 2). A dilute particle suspension (0.003 wt%) in 0.001 M KCl at pH 9, with or without CMC, was gently poured into the lower section of the flotation column. The top part of the column was then filled with the background electrolyte. The three-way valve was then opened (position ‘B’ in Figure 2) so that the graphite particle suspension came into contact with the background electrolyte above it. At this point the bubbles were generated by the same microfluidic chip as used in the bubble collision apparatus. This approach ensures that the same bubble size was used, and that precise control was maintained over the frequency of bubble generation. A single bubble was released every 30-60 s, ensuring adequate spacing between subsequent bubbles. 200 bubbles were generated and allowed to rise to the top of the Hallimond tube. The solution in the Hallimond tube concentrate receiver was collected and analysed in terms of number and size of floated particles.

In order to ensure that all the experiments were conducted in a clean (relatively particle-free) system, a blank ‘flotation’ test was carried out prior experiments. In such a test, both the

bottom and top columns were filled with the background electrolyte solution. If the number of particles collected in such experiment was less than 30 per 1 mL of the concentrate, the Hallimond tube was considered clean. The background values were subtracted from the collection data in further experiments.

The flotation recovery is expressed in terms of the particle–bubble collection efficiency, E_{coll} , and is defined as⁵¹:

$$E_{coll} = \frac{N_{pf}}{PNC\pi h_s(d_p+d_b)^2/4} \quad (3)$$

where N_{pf} is the number of particles collected per bubble, PNC is the number of particles in that size fraction per cm^3 , h_s is the height of suspension, d_p and d_b are particle and bubble diameters, respectively.

Particle Number and Size Determination: An Accusizer C770 Optical Particle Sizer (Particle Sizing Systems, Inc., USA) was used for the particle number determination and sizing. The Accusizer combines light scattering and light obscuration to allow measurement in the range of particle sizes from 0.5 μm to 500 μm . Light scattering, in which a single particle scatters light with an angular dependence dependent on its diameter and relative refractive index, is used for particles up to several microns. For larger particles a light obscuration, or blockage methodology, is used. In the latter case, a particle passing through a narrow area of uniform illumination causes a fraction of the illuminating beam to be blocked or deflected away by an amount approximately equal to the cross-sectional area of the particle.

Cleaning: A microfluidic chip with two channels in a T-geometry was used to generate air bubbles of well-defined sizes. Prior to experiments, the channels were flushed for 30 min with 2% Hellmanex (Hellma Analytics, Germany) in Milli-Q water solution and, Milli-Q

water for another 30 min. At the end, 1 M KOH was flushed for 30 min. Milli-Q water was then pumped until neutral pH was reached. For all of the above steps the flow rate was kept constant and equal to 4 mL h^{-1} . The channels were then dried by pumping air through the system. The AFM quartz liquid cell was first soaked in ethanol (AR, 99.5%, Chem-Supply, Australia) for 30 min, rinsed with Milli-Q water for 30 min, and then soaked in 1 M KOH for another 30 min. It was then rinsed with Milli-Q water until neutral pH was reached, dried with a nitrogen gun and kept in a laminar flow cabinet prior the experiments. AFM cantilevers were cleaned by soaking them in ethanol, rinsing with Milli-Q water and (when dried) by exposing them to air plasma in a plasma cleaner (Harrick, PDC-OD2, USA) for 60 s.

All glassware was soaked in 5% Extran® MA05 (Merck Millipore, USA) in deionised water solution for 2 h, then rinsed well with deionised water and placed in 1 M KOH aqueous solution for 2 h. All the glassware was then rinsed with Milli-Q water until neutral pH was reached. Prior to each experiment, the borosilicate glass column and the Pyrex glass microfluidic chips were cleaned with air plasma in a plasma cleaner for 60-90 s. All Teflon parts and Hamilton Gastight® syringes (Hamilton, USA) were sonicated in 2% Hellmanex in Milli-Q water solution for 15 min, then rinsed with Milli-Q water and sonicated in Milli-Q for another 15 min. Teflon parts and the syringes were then dried with nitrogen gun and exposed to plasma for 60-90 s.

RESULTS AND DISCUSSION

Topography of CMC-modified HOPG Surfaces:

AFM is a powerful technique for imaging polymers adsorbed onto atomically smooth surfaces. It provides good lateral resolution and gives precise height information. AFM height images of CMC adsorbed from the solution onto freshly cleaved HOPG surface are shown in

Figure 3. Top and bottom panels on the left present $1 \times 1 \mu\text{m}^2$ and $500 \times 500 \text{ nm}^2$ height images acquired *in situ* after 30 min of immersion in $5 \text{ mg}\cdot\text{L}^{-1}$ CMC in 0.001 M KCl at pH 9 solution, respectively. Top and bottom panels on the right present $1 \times 1 \mu\text{m}^2$ and $500 \times 500 \text{ nm}^2$ height images acquired *in situ* after 30 min of immersion in $25 \text{ mg}\cdot\text{L}^{-1}$ CMC in 0.001 M KCl at pH 9 solution, respectively. Images acquired for lower CMC concentration show extended chains, randomly and sparsely distributed all over the HOPG surface, with no preferential adsorption at the basal plane or at the edge of HOPG. Ueno *et al.* also reported a stretched chain-net morphology of CMC, adsorbed from $10 \text{ mg}\cdot\text{L}^{-1}$ CMC in 0.01 M NaCl on an HOPG surface⁵². They reported that CMC chains (at a mono-chain level, with an average height of 1.1 nm) were covering a significant surface area (30-35%); the CMC chains were possibly aligned along the HOPG crystal lattice⁵². In our study however, there are significant differences in the AFM images compared to this earlier work (see left panels of Figure 3): (i) CMC chains cover only small part of HOPG surface ($\sim 2 \%$), (ii) there is no specific order in the way CMC chains adsorbed, (iii) the distance between chains is much larger than the distance observed by Ueno *et al.*⁵², (iv) there is a distribution in the vertical profiles of the single and overlapping CMC chains (while Ueno *et al.* report ‘...all the height data of the CMC chains coincide well with ca. 1.1 nm on the HOPG surface...’). The first three differences can be explained by the difference in the ionic strength of the background electrolyte solution. Ueno *et al.* used 0.01 M NaCl, while 0.001 M KCl is used in this study. Both NaCl and KCl are simple monovalent salts and unless there is specific adsorption of Na^+ or K^+ ions to the surface of HOPG, there should be no significant difference in the way CMC adsorbs from these electrolytes onto HOPG. However, the ionic strength used in the two studies varies by an order of magnitude. This affects not only the magnitude of the zeta potential of CMC ($-45.7 \pm 7.1 \text{ mV}$ for ionic strength of 0.01 M, and $-62.5 \pm 4.8 \text{ mV}$ for

ionic strength of 0.001 M^e), but also the Debye length (κ^{-1} is 3.04 nm for ionic strength of 0.01 M, and 9.62 nm for ionic strength of 0.001 M). This is why in 0.01 M NaCl the electrostatic repulsive interactions between CMC chains will be weaker and of shorter length. Such screening will result in denser CMC adsorption and thus higher surface coverage.

The last difference, i.e. the difference in the distribution in the vertical profiles of the single and overlapping CMC chains is most likely a result of the adsorption time (Ueno *et al.* used extremely short adsorption time – 3 s, while in our studies the adsorption time was 30 min, before thorough rinse with 0.001 M KCl at pH 9^f). Some height profiles (extracted from $2 \times 2 \mu\text{m}^2$ AFM height image) of a single and overlapping CMC chains are presented in Figure S11. The limits of the height distribution (determined from multiple cross-sections for single chains of CMC) are 0.7 and 1.4 nm, while the limits of height distribution for overlapping chains of CMC are 0.9 and 1.7 nm.

Much more complex topographical images are acquired after 30 min of HOPG immersion in $25 \text{ mg}\cdot\text{L}^{-1}$ CMC in 0.001 M KCl at pH 9 solution (see right panels of Figure). The CMC polymer forms an interconnected network of multilayer features (the network of CMC chains adsorbed at the HOPG surface, and clusters of ordered chains (the chains are parallel to each other within one cluster, but this ‘ordering’ varies for different clusters). The multilayer features may be due to the cellulose polymer backbone ordering similarly to that seen in cellulose crystals, with the saccharide rings lying flat on an underlying hydrophobic surface (initial layer of CMC), and undergoing lateral hydrogen bonding interactions^{53,36}.

^e As determined from electrophoretic mobility measurements (Zetasizer Nano ZS, Malvern, USA).

^f Although Ueno *et al.*⁶⁷ claim that ‘longer (than 3 s) contact time brought about the excessive adsorption of CMC molecules and their assembly, resulting in an obscure molecular imaging because of the overall coverage of the HOPG surface’ we do not see it in our *in situ* AFM images acquired after 30 min of immersion in $5 \text{ mg}\cdot\text{L}^{-1}$ CMC in 0.001 M KCl at pH 9 solution.

Zeta potential of CMC-modified HOPG Surfaces:

Since the CMC molecules are charged, the adsorption of CMC will alter the average value of zeta potential of the HOPG surface. The average zeta potential of HOPG in 0.001 M KCl at pH 9 is determined to be -42.8 ± 1.3 mV. It is well-known that the edges and basal planes of HOPG bear different (in magnitude and origin) surface potential. The negative surface potential of the edges results from oxidised carbon functional groups (most likely carboxyl). However the basal plane of the pristine HOPG has no functional groups which could dissociate and contribute to surface charging, and the negative charge most likely arises from specific adsorption of OH^- ions, in analogy to that which occurs at air bubble, oil droplet, and at non-polar fluoropolymer interfaces^{54, 55 56}.

Upon adsorption of CMC onto the HOPG surface, the zeta potential^g becomes more negative. The zeta potential determined in 0.001 M KCl at pH 9 after 30 min of adsorption from $5 \text{ mg}\cdot\text{L}^{-1}$ CMC solution was -51.7 ± 0.7 mV and the zeta potential determined in 0.001 M KCl at pH 9 after 30 min of adsorption from $25 \text{ mg}\cdot\text{L}^{-1}$ CMC solution was -58.1 ± 1.4 mV. The higher negative surface potential originates from the carboxymethyl groups of the CMC polymer. These groups are fully dissociated and negatively charged above pH 6³³. The increase in magnitude of zeta potential with increase of CMC concentration indicates greater adsorption of CMC onto HOPG surface, which is in a good agreement with AFM topographic data.

Wetting Film Drainage and Stability: Bare HOPG surfaces

A representative bubble collision with freshly cleaved HOPG in 0.001 M KCl at pH 9 is presented as a sequence of frames in Figure 4. The bubble approaches the electrolyte-HOPG interface (see first 5 frames of panel A in Figure 4), ‘touches’ it (see frame number 6 of panel

^g Since CMC does not form a uniform monolayer the determined zeta potential is an average value of the zeta potential over the non-modified (bare) and CMC-modified HOPG surface.

A in Figure 4) and a wetting film forms between the bubble-water interface and the HOPG-water interface. The film starts to drain (see frames 6 - 9 of panel A in Figure 4), and once the critical thickness of rupture is reached, the wetting film ruptures and a TPCL is formed (see frame 1 of panel B in Figure 4). The diameter of the TPCL expands until it reaches its static (final) value (see frames 2 - 9 of panel B in Figure 4 and the diameter of dewetted perimeter as a function of time in Figure 5). In the case of freshly cleaved HOPG the film drainage is a very quick process (on average 5.2 ± 2.8 ms), the film rupture is very rapid (less than 1 ms), and dewetting takes only few ms (7.9 ± 3.9 ms). In addition to rapid bubble attachment, the static receding contact angle is relatively high ($66.9 \pm 4.1^\circ$), indicating that: (i) the wetting film on such a solid is not stable, and (ii) such a hydrophobic solid would float very well.

The drainage and stability of the wetting film is governed by the hydrodynamics (repulsive in nature) of the system and the interfacial forces (that can be either repulsive or attractive) across the film, respectively. If the resultant total force across the film is attractive, the film becomes unstable, and the drainage is followed by a film rupture.

Classically, to calculate the rate of thin film thinning in terms of the film thickness, h_f , as a function of time, t , the Stefan-Reynolds equation, which models the bubble or droplet and a solid interface as two parallel discs being pushed against each other together with a total (gravity-driven) force, F_b , causing the film thinning, is employed⁵⁷. Scheludko and Platikanov implemented the approach to describe the thinning of a circular plane parallel film between a solid wall and a free solution-gas interface by the relation^{58,59}:

$$\frac{1}{h_f^2} = \frac{4m}{3} \frac{\Delta p}{\nu R_f^2} t + \frac{1}{h_i^2} \quad (4)$$

The effective radius of the film, R_f , formed by a bubble at the interface is expressed by⁶⁰:

$$R_f^2 = \frac{F_b R_b}{2\pi\gamma} \quad (5)$$

where R_b is the bubble radius. Taking into account that $\Delta p = \frac{2\gamma}{R_b}$ and $F_b = \frac{4}{3}R_b^3\rho g$, the final expression for the wetting film thinning can be written as⁶¹:

$$\frac{1}{h_f^2} = 4m \frac{\gamma^2}{\nu\rho g R_b^5} t + \frac{1}{h_i^2} \quad (6)$$

where m is the mobility parameter at the solution-gas interface (for a wetting film with zero velocity at both interfaces, m equals 1; for a wetting film between a solid-solution interface with no-slip and a fully mobile solution-gas interface, m equals 4), ρ is the solution density, g is the acceleration due to gravity, and h_i is the initial film thickness.

The wetting film thickness depends on several factors, including: physicochemical properties of the fluid phases, hydrodynamic boundary conditions (BC) at the solution-gas interface^h (with the film reaching the same thickness faster when a full slip BC occurs at the solution-gas interface), bubble radius (with the film reaching the same thickness faster when for smaller bubbles), and initial film thickness. From the bubble terminal velocity measurements and the comparison with the model of Klaseboer *et al.* we can conclude that the solution-air interface is fully mobile, thus $m = 4$. The experimentally measured film drainage time, i.e. the time from the moment when the bubble does not move further beneath the HOPG surface (within the lateral resolution limit of the stereo microscope and high speed video camera) until the film starts to rupture, between an air bubble and freshly cleaved HOPG surface in 0.001 M KCl at pH 9 as a function of the bubble diameter, is presented in Figure 6. The drainage time increases with the bubble diameter and equals: 2.3 ± 1.3 ms (average value of drainage time calculated for the first cluster of experimental points in Figure 6) for bubble diameters 414 – 425 μm , 5.2 ± 1.3 ms (average value of drainage time

^h Equation (5) assumes no-slip (e.g. zero velocity) at the solid-solution interface, however it has been experimentally proven that slip occurs on hydrophilic⁵⁶ and hydrophobic⁵⁷ surfaces, moreover very large slip lengths at hydrophobic solid-solution interface can be attributed to the presence of gas features at the interface⁵⁸. For this reasons the film may drain even faster than predicted by Equation (5) and the film thickness may be overestimated.

calculated for the second cluster of experimental points in Figure 6) for bubble diameters 429 – 437 μm , and 8.7 ± 1.5 ms (average value of drainage time calculated for the third cluster of experimental points in Figure 5 for bubble diameters 443 – 448 μm . Knowing the time of film drainage, and using Equation (6), one can estimate the wetting film thickness upon its rupture. Assuming that there is no detectable change in the position of the bubble top pole, the film should not be thicker than 1 pixel. Thus, the initial film thickness should not be larger than ~ 4 μm . The lower limit of the initial film thickness is chosen to be an order of magnitude lower, i.e. 400 nm. The film thickness versus time for these two limiting cases is presented and compared in Figure SI2. The calculated film thickness upon its rupture for bubbles of diameter 419 μm (and the average drainage time 2.3 ms) is between 128 nm (for $h_i = 400$ nm) and 135 nm (for $h_i = 4$ μm), the calculated film thickness upon its rupture for bubbles of diameter 433 μm (and the average drainage time 5.2 ms) is between 94 nm (for $h_i = 400$ nm) and 97 nm (for $h_i = 4$ μm), and the calculated film thickness upon its rupture for bubbles of diameter 446 μm (and the average drainage time 8.7 ms) is between 79 nm (for $h_i = 400$ nm) and 81 nm (for $h_i = 4$ μm). The calculated film thickness values indicate that the choice of the initial film thickness is only critical for the first couple of ms, and for longer drainage times the difference in the calculated film thickness is small. The calculated film thicknesses for longer drainage times (5.2 and 8.7 ms) are comparable with the experimentally measured critical thickness of rupture of the wetting films on hydrophobised titania surfaces (of static advancing contact angles, $\theta_{\text{adv}} = 40$ and 60°)⁶¹.

The DLVO (named after Derjaguin, Landau, Verwey and Overbeek⁶⁵) interfacial forces between HOPG and an air bubble in 0.001 M KCl at pH 9 are composed of the repulsive van der Waals (the Hamaker coefficient for carbon-water-air system is negative: $-5.68 \cdot 10^{-20}$ J⁶⁶) and the repulsive electrostatic (zeta potential of HOPG is -42.8 ± 1.3 mV, zeta potential of air bubble is ~ -50 mV⁶⁷, and the Debye length, κ^{-1} , is 9.62 nm) interactions. Repulsive

components of interfacial forces should stabilise the wetting film (at thickness of a few tens of nm, as indicated by κ^{-1}) preventing bubble attachment to HOPG surface. However: (i) from Equation (6) we estimate that the film ruptures at thicknesses much greater than the thickness at which interfacial forces are operational, (ii) air in the form of nano-/submicron-bubbles can be present at the HOPG-solution interface. The presence of nanobubbles at HOPG surfaces is well documented^{68,69}. It is also probable that there is air entrapment (in form of submicrometer features) at the hydrophobic solid-solution interface during the substrate immersion into an aqueous phase^{5, 70}. In such a case, the macroscopic bubble is in contact with nano-/submicroscopic bubbles nucleated/attached to HOPG-solution interface, rather than pristine HOPG-solution interface. Even though the electrostatic interaction between two bubbles across thin aqueous film is still repulsive, the van der Waals interaction becomes attractive (the Hamaker coefficient for air-water-air system is positive: $3.7 \cdot 10^{-20} \text{ J}^{65}$). This can lead to the destabilisation of the film (at wetting film thicknesses larger than predicted by DLVO forces, as the height of the nanobubbles are in the range of 10 - 80 nm⁷¹ with a typical value of 20 - 30 nm⁷²), followed by the film rupture and the bubble attachment.

Wetting Film Drainage and Stability: CMC-modified HOPG surfaces

The sequence of images presenting the bubble attachment and the dewetting process for CMC-modified HOPG surfaces are presented in Figures 7A (for HOPG modified by $5 \text{ mg} \cdot \text{L}^{-1}$ CMC solution) and 7B (for HOPG modified by $25 \text{ mg} \cdot \text{L}^{-1}$ CMC solution), for representative collisions for both conditions. The first significant difference between freshly cleaved (non-modified) HOPG and CMC-modified HOPG is the drainage time. The drainage times (t_d) of the wetting film formed between the air bubble and CMC-modified HOPG surface are significantly longer (for the cases illustrated in Figures 7A and 7B, the drainage times are 18 and 66 ms for HOPG modification from 5 and $25 \text{ mg} \cdot \text{L}^{-1}$ CMC solutions, respectively). The

average drainage times, calculated from 30-50 experiments for each system are plotted in Figure 8. The average t_d for the wetting film between an air bubble and freshly cleaved HOPG is 5.2 ± 2.8 ms. The average values of t_d for the wetting films between an air bubble and CMC-modified HOPG are longer, and equal: 17.5 ± 7.2 ms for HOPG modified by $5 \text{ mg}\cdot\text{L}^{-1}$ CMC solution, and 64.1 ± 7.2 ms. This prolongation of the drainage time with CMC adsorption may originate from two factors: (i) the CMC modified HOPG surface is less hydrophobic (it is clearly seen from the sequence of frames in Figures 4 and 7 that the receding contact angles are much lower for CMC-modified HOPG surface), and therefore the interaction of water molecules with the CMC-modified HOPG surface is stronger (i.e. more tightly hydrated), and the velocity of water molecules at the solution-solid interface (which will alter the drainage speed) is lower, or approaching zero; (ii) the magnitude of the zeta potential increases with the CMC adsorption: the average value of zeta potential for freshly cleaved HOPG surface is -42.8 ± 1.3 mV, while for CMC-modified HOPG surface it is -51.7 ± 0.7 mV and -58.1 ± 1.4 mV for CMC adsorption from 5 and 25 $\text{mg}\cdot\text{L}^{-1}$ solutions, respectively. The increase in zeta potential translates into a stronger repulsive electrostatic interactions (see Figure SI3) which could cause slower drainage.

Another distinct difference between the bubble-surface collisions for bare and CMC-modified HOPG surfaces is the dewetting kinetics, which can be expressed in terms of receding contact angle as a function of time. Comparing the frames in Figure 7 and the contact angle data presented in Figure 9 (two datasets presented for the polymer-treated HOPG, to give an indication of the variation between collisions), one can see that the receding contact angle is lower for CMC-modified HOPG surfaces and that it further decreases with the increase in CMC concentration. When the wetting film ruptures ($t = 0$ ms in Figures 4 and 7) the TPCL is formed ($t = 1$ ms in Figures 4 and 7) and the bubble attaches to the solid surface forming a specific receding contact angle. This receding contact angle

changes with time, reaching at the end its static value. For the bare HOPG and CMC-modified HOPG surfaces shown in Figures 4 and 7, the receding contact angle changes at different rates, for example at $t = 1$ ms, $\theta_{\text{rec}} = 65.4^\circ$ for bare HOPG, $\theta_{\text{rec}} = 46.4^\circ$ for $5 \text{ mg}\cdot\text{L}^{-1}$ CMC-modified HOPG (a 19.0 degrees drop in respect to bare HOPG) and $\theta_{\text{rec}} = 17.8^\circ$ for $25 \text{ mg}\cdot\text{L}^{-1}$ CMC modified HOPG (a 47.6 degrees drop in respect to bare HOPG). At $t = 10$ ms the difference in the receding contact angle between bare and CMC-modified HOPG surfaces gets smaller: $\theta_{\text{rec}} = 67.7^\circ$ for bare HOPG, $\theta_{\text{rec}} = 52.3^\circ$ for $5 \text{ mg}\cdot\text{L}^{-1}$ CMC-modified HOPG (a 15.4 degrees drop in respect to bare HOPG) and $\theta_{\text{rec}} = 26.0^\circ$ for $25 \text{ mg}\cdot\text{L}^{-1}$ CMC-modified HOPG (a 41.7 degrees drop in respect to bare HOPG). The difference further decreases with the increase in the dewetting time, for $t = 100$ ms $\theta_{\text{rec}} = 68.3^\circ$ for bare HOPG, $\theta_{\text{rec}} = 54.8^\circ$ for $5 \text{ mg}\cdot\text{L}^{-1}$ CMC-modified HOPG (a 13.5 degrees drop in respect to bare HOPG) and $\theta_{\text{rec}} = 30.8^\circ$ for $25 \text{ mg}\cdot\text{L}^{-1}$ CMC-modified HOPG (a 37.5 degrees drop in respect to bare HOPG). The average values of the static receding contact angle for all three studied systems are compared in Figure 8. The highest static receding contact angles are recorded on bare HOPG, indicating this is the most hydrophobic of all the three substrates. The average value of static θ_{rec} on bare HOPG is $66.9 \pm 4.1^\circ$. The static receding contact angle is significantly smaller for CMC-modified HOPG surfaces: static θ_{rec} for $5 \text{ mg}\cdot\text{L}^{-1}$ CMC-modified HOPG is $51.5 \pm 7.8^\circ$, and static θ_{rec} for $25 \text{ mg}\cdot\text{L}^{-1}$ CMC-modified HOPG is $31.4 \pm 6.3^\circ$. The difference between these three systems can be also noted in the spreading time, i.e. the time from the moment when the wetting film ruptures, until the time when the receding contact angle reaches its static value. The average values of the spreading time for all three studied systems are compared in Figure 8. The spreading time on HOPG equals 7.9 ± 3.9 ms, the spreading time for $5 \text{ mg}\cdot\text{L}^{-1}$ CMC-modified HOPG is significantly longer than on bare HOPG and equals 67.3 ± 28.2 ms. The longest spreading times were recorded for $25 \text{ mg}\cdot\text{L}^{-1}$ CMC-modified HOPG: 249.0 ± 41.5 ms.

The dynamic dewetting of surfaces is often plotted as a function of the logarithm of the dewetting time. This data is shown in Figure 10A for graphite in the presence of CMC adsorbed at the two different concentrations. The two datasets shown in Figure 10A were further processed using the G-Dyna program⁴⁸. This allowed for the extraction of the dynamic receding contact angle versus contact line velocity, and this data is shown Figure 10B. This representation of the dynamic dewetting allows for analysis using MKT. The fitting based on Equation (2) is used to extract the MK model parameters for the two cases for CMC-modified HOPG surfaces. The fitted curves from the MK model analysis are also given in Figure 10B. For HOPG exposed to $5 \text{ mg}\cdot\text{L}^{-1}$ CMC, the fitting parameters (k_0 – jump frequency; λ_{MK} – jump length) for the two datasets are: dataset 1 – $k_0 = 14.4 \pm 1.9 \text{ kHz}$, and $\lambda_{\text{MK}} = 2.61 \pm 0.06 \text{ nm}$; dataset 2 – $k_0 = 26.7 \pm 4.0 \text{ kHz}$, and $\lambda_{\text{MK}} = 2.30 \pm 0.07 \text{ nm}$. For HOPG exposed to $25 \text{ mg}\cdot\text{L}^{-1}$ CMC, the fitting parameters for the two datasets are: dataset 1 – $k_0 = 1.6 \pm 0.2 \text{ kHz}$, and $\lambda_{\text{MK}} = 3.91 \pm 0.06 \text{ nm}$; dataset 2 – $k_0 = 3.1 \pm 0.4 \text{ kHz}$, and $\lambda_{\text{MK}} = 3.28 \pm 0.06 \text{ nm}$. Note: the λ_{MK} and k_0 distribution plots from the full set of MK fitting procedures (see experimental section) for both plotted datasets from each polymer concentration are given in the supplementary information (Figure SI4 and Figure SI5)

The average MK model parameters for these fitting procedures are given in Table 1, along with a summary of the average parameters from the bubble-surface collisions under the various conditions. In both cases, the average jump length is much larger than the solvent molecule dimensions, implying the movement of solvent clusters across the surface during the dewetting. This magnitude of jump length has also been observed in previous studies of water displacement by air, in studies of bubble attachment to hydrophobised titania⁴ and on roughened n-heptyl amine⁷³. The change in jump length observed in this work with altered CMC concentration, i.e. an increase that correlates with greater coverage of CMC, and thus

lower hydrophobicity, is also in agreement with the observed increase in jump length associated with decreased hydrophobicity for OTHS-coated titania⁴.

The fitting procedure indicates that there is a marked reduction in the jump frequency for the HOPG coated from 25 mg·L⁻¹ CMC solution relative to the HOPG coated from 5 mg·L⁻¹ CMC solution. The most common interpretation of variation in jump frequency for a given liquid on different substrates is that high jump frequencies represent solvent-substrate systems of low affinity (i.e. in this case, more hydrophobic surfaces). This interpretation is based on the relationship between the jump frequency and the work of adhesion (e.g. see equation 15 in⁷⁴). Thus it would be expected that the HOPG coated from 25 mg·L⁻¹ CMC, which has a lower hydrophobicity and near-complete layer of hydrated polymer chains, would give rise to a lower jump frequency due to the affinity of the solvent (water) for the dominant exposed surface (hydrated CMC chains). However, given the complex surface morphology of the CMC adsorbed layer on the two HOPG surfaces (varying roughness, varying coverage), there is the possibility that surface inhomogeneity is also affecting the dewetting process and MK model parameters^{73,75}.

Table 1. Effect of CMCs on drainage time and final receding contact angle of bare HOPG and polymer-modified HOPG. MK model parameters (λ_{MK} and k_0) are also given for the polymer-modified HOPG dewetting examples (average of the two determined values from the fitting procedures for the two datasets for each polymer concentration).

HOPG	t_d [ms]	θ_{rec} [degrees]	λ_{MK} [nm]	k_0 [kHz]
Bare	5.23 ± 2.8	66.9 ± 4.1	ⁱ	-
5 mg·L ⁻¹ CMC	17.5 ± 7.2	51.5 ± 7.8	2.45	20.5
25 mg·L ⁻¹ CMC	64.1 ± 19.2	31.4 ± 6.3	3.60	2.3

ⁱ The dewetting process for bare HOPG is too rapid. No reliable MK model parameters can be extracted for bare HOPG surfaces.

Single Bubble Hallimond Tube Flotation:

Collection efficiencies (calculated from Equation (3)) for bare and CMC-modified graphite particles are presented in Figure 11. Collection efficiency is the highest for bare graphite particles – this is in a good agreement with the shortest t_d and the TPCL spreading times, as well as the highest receding contact angle obtained from bubble-surface collision experiments. E_{coll} is seen to increase with the particle size. Lower E_{coll} values were calculated for graphite particles modified with CMC solution of lower concentration. The difference gets larger with the particle size. The lowest E_{coll} values (and a reversed trend with increasing particle size. i.e. E_{coll} , decreasing with the particle size), were observed for graphite particles modified with CMC solution of higher concentration. The decrease in E_{coll} values upon polymer adsorption indicates that the bubble-particle attachment is inhibited. This could be due to higher drainage time, longer spreading of the TPCL or insufficient hydrophobicity (or, most probably, due to the sum of all these parameters). The decrease in E_{coll} with particle size is due to low receding contact angles. When the film ruptures and the TPCL expands, the diameter of the dewetting perimeter is a function of the receding contact angle. For lower receding contact angles the diameter of the dewetting perimeter is small, and thus not large enough for the formation of a stable bubble-particle aggregate. Larger particles will detach from the bubble due to gravity.

CONCLUSIONS

The morphology of CMC adsorbed onto HOPG surface from solutions of different concentration differs significantly. In addition, the zeta potential of HOPG surface changes with the adsorption of CMC, with the zeta potential becoming more negative with the higher adsorption of CMC. These variations in both the morphology and the electric state of the adsorbed layer are seen to have a profound effect on the ability of the polymer layer to slow

down bubble-particle attachment. The quantification of the bubble collisions and spreading process has revealed that for a HOPG surface of lower CMC coverage and smaller negative zeta potential, the time of film drainage was shorter and the spreading of the TPCL was faster. In addition, receding contact angles were higher. The jump frequencies extracted from the MK model were an order of magnitude higher for this case, indicating weaker interactions between water molecules and the HOPG surface sparsely covered with CMC chains. Collection efficiencies for CMC-modified graphite particles were also distinctly lower than for bare graphite. In addition, for bare graphite and graphite particles modified by adsorption of CMC from the solution of lower concentration, the collection efficiency was increasing with particle size, while the opposite trend, i.e. the collection efficiency decreasing with the particle size was observed for graphite particles modified by adsorption of carboxymethylcellulose from the solution of higher concentration. The switch in behavior for the two cases of adsorbed CMC highlights the importance of significant coverage on the alteration of bubble-surface interactions.

ACKNOWLEDGMENT: The authors would like to thank: Joel De Coninck (Université de Mons, Belgium) for providing G-Dyna software; Audrey Beaussart for the graphite SEM image and photograph of a water droplet on HOPG in Figure 1. Financial support for was received from the Australian Research Council (Linkage Project LP0990646, Future Fellowship FT100100393, Discovery Project DP110104179). This work was performed in part at the South Australian node of the Australian National Fabrication Facility, a company established under the National Collaborative Research Infrastructure Strategy to provide nano- and micro-fabrication facilities for Australia's researchers.

Electronic Supplementary Information Available: The film drainage calculated from Equation (6) for HOPG-air bubble system; AFM height profiles along the cross-sections of single and overlapping CMC chains; the normalised (in respect to bubble radius) interaction forces between an air bubble and bare and CMC-modified HOPG surfaces. This material is available free of charge via the Internet at www.rsc.org/softmatter

FIGURES

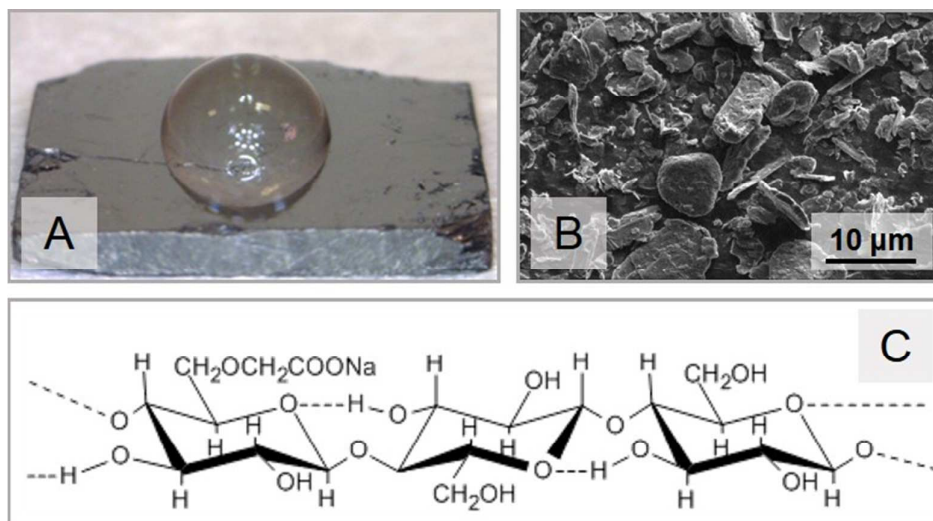


Figure 1. (A) photograph of HOPG sample type used for AFM imaging, zeta potential determination, and bubble-surface collisions (with water droplet); (B) SEM image of graphite particles used in single bubble Hallimond tube flotation experiment; (C) chemical structure of CMC (adapted from Coultate⁷⁶).

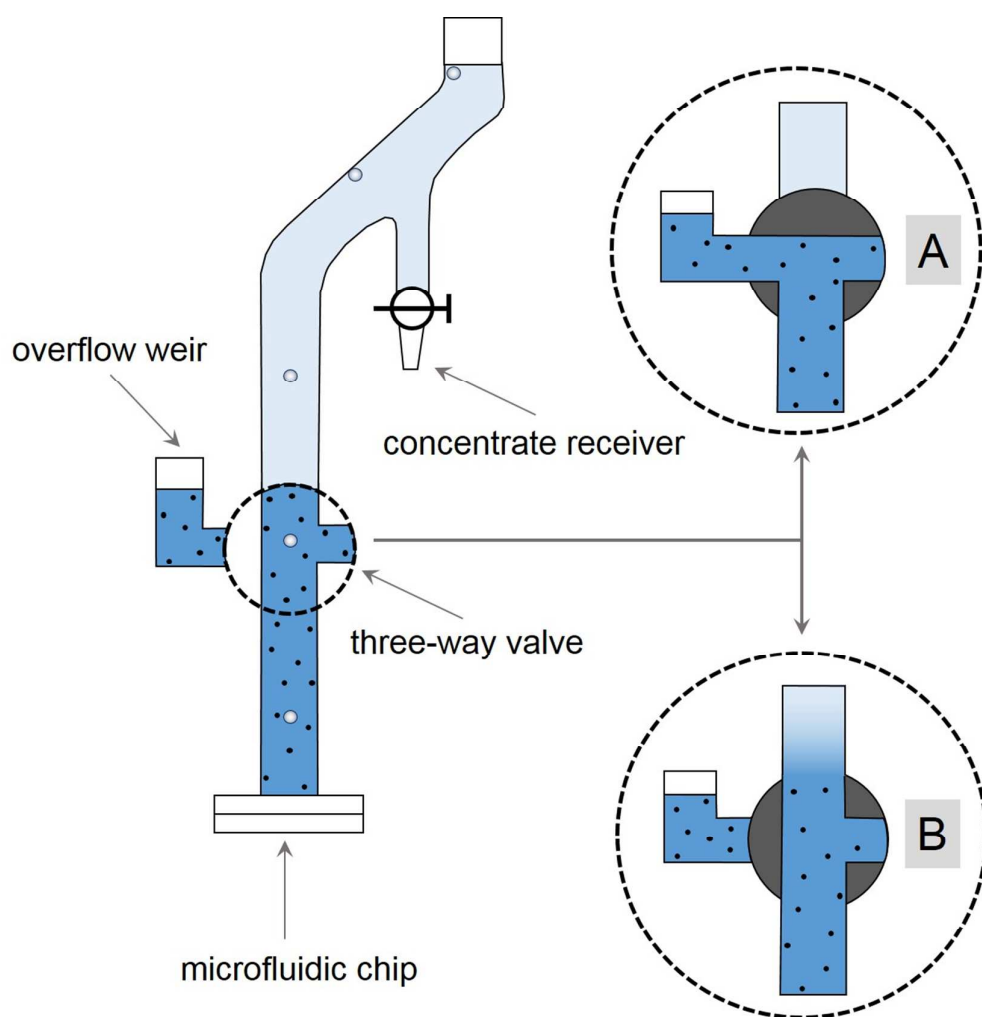


Figure 2. Schematic representation of the modified Hallimond tube for single bubble flotation. (A) the position of three-way valve during feeding and after flotation; (B) the position of three-way valve during flotation.

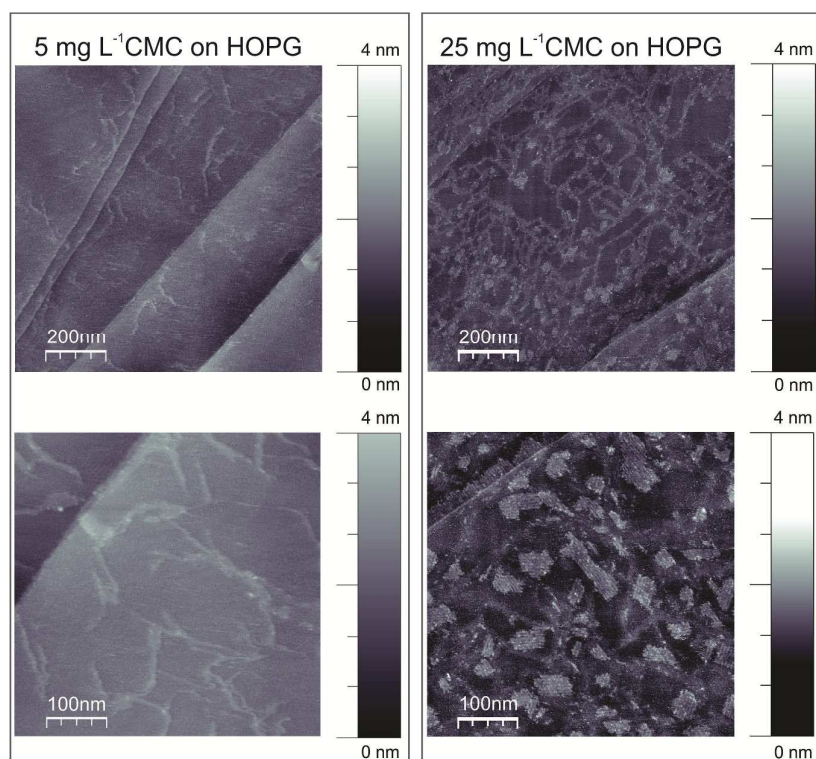
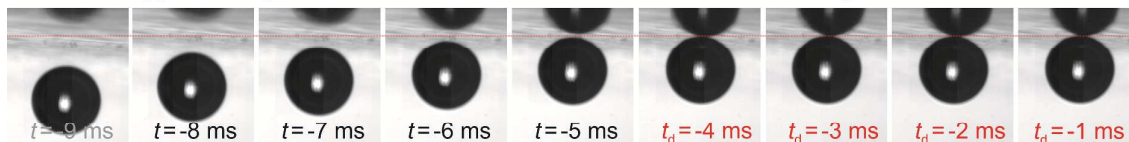


Figure 3. Left column: $1 \times 1 \mu\text{m}^2$ (top) and $500 \times 500 \text{ nm}^2$ (bottom) height images acquired *in situ* after 30 min of immersion in $5 \text{ mg}\cdot\text{L}^{-1}$ CMC solution; right column: $1 \times 1 \mu\text{m}^2$ (top) and $500 \times 500 \text{ nm}^2$ (bottom) height images acquired *in situ* after 30 min of immersion in $25 \text{ mg}\cdot\text{L}^{-1}$ CMC solution.

A. Bubble approaching the solution-HOPG interface and thin film drainage



B. Thin film rupture and the TPCL expansion

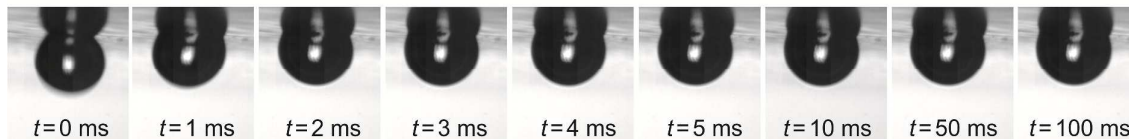


Figure 4. Sequence of images showing the collision (panel A) and attachment (panel B) of a rising bubble ($d_b = 433 \mu\text{m}$) to a freshly cleaved HOPG surface; 0.001 M KCl, pH 9.

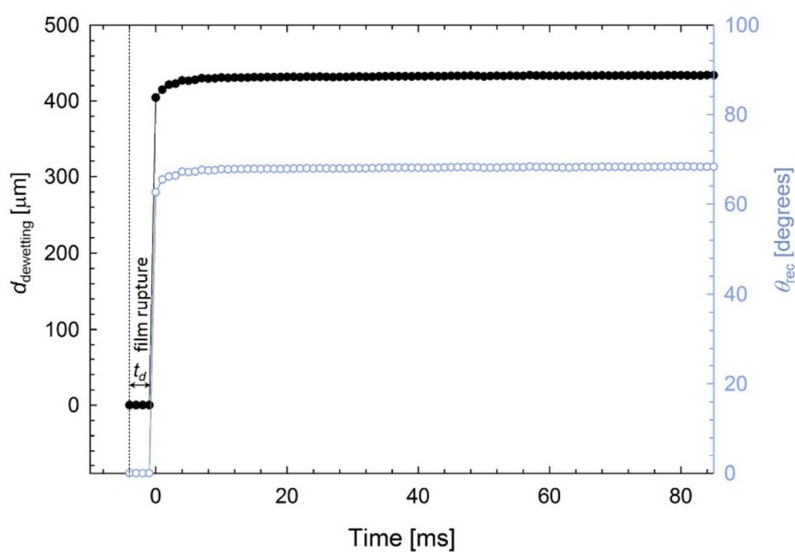


Figure 5. Diameter of the dewetted perimeter, $d_{\text{dewetting}}$, (full circles) and dynamic receding contact angle (open circles) as a function of time for bare, freshly cleaved HOPG surface; $d_b = 433 \mu\text{m}$; 0.001 M KCl, pH 9.

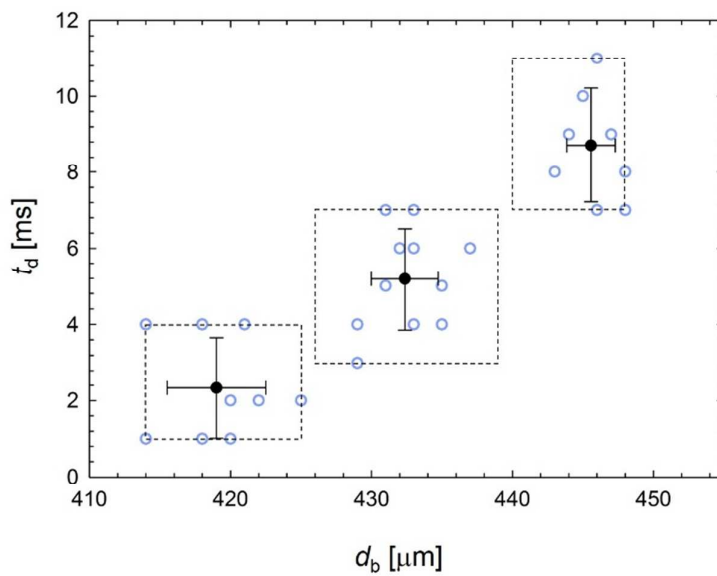


Figure 6. Wetting film drainage time between air bubble and freshly cleaved HOPG surface, as a function of bubble diameter. Open circles are experimental data, and full circles are the average values for each of the experimental data clusters. The experiments were carried out in 0.001 M KCl at pH 9.

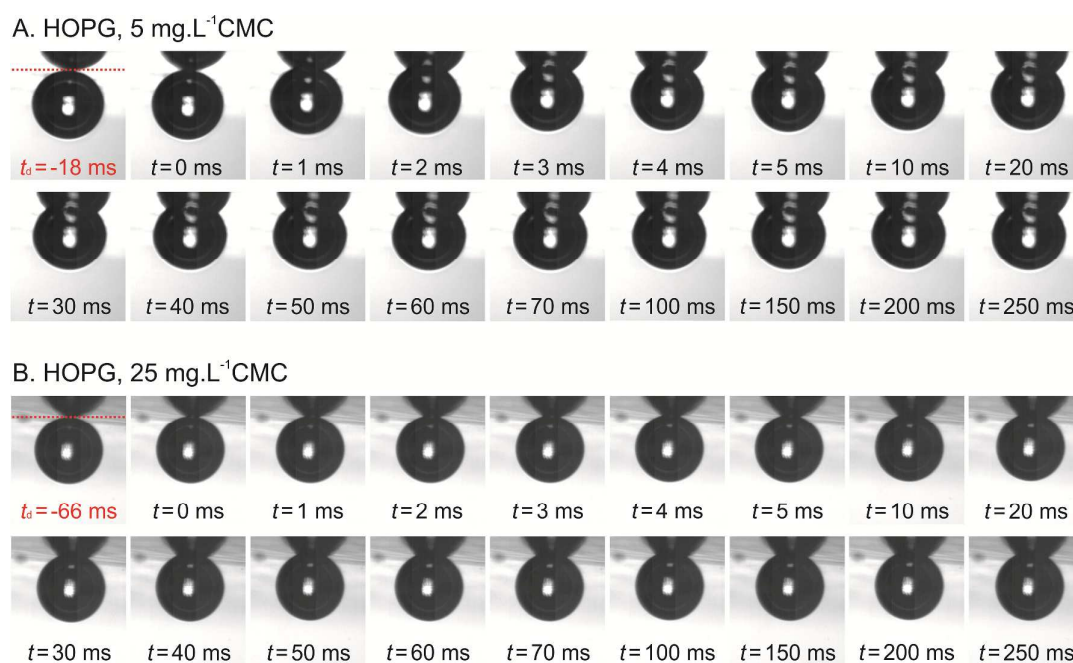


Figure 7. Sequence of images showing the film rupture, bubble attachment and dewetting on CMC-modified HOPG surface in 0.001 M KCl, pH 9. Panel A - after HOPG treatment in 5 mg·L⁻¹ CMC solution ($d_b = 448 \mu\text{m}$); Panel B - after HOPG treatment in 25 mg·L⁻¹ CMC solution ($d_b = 441 \mu\text{m}$).

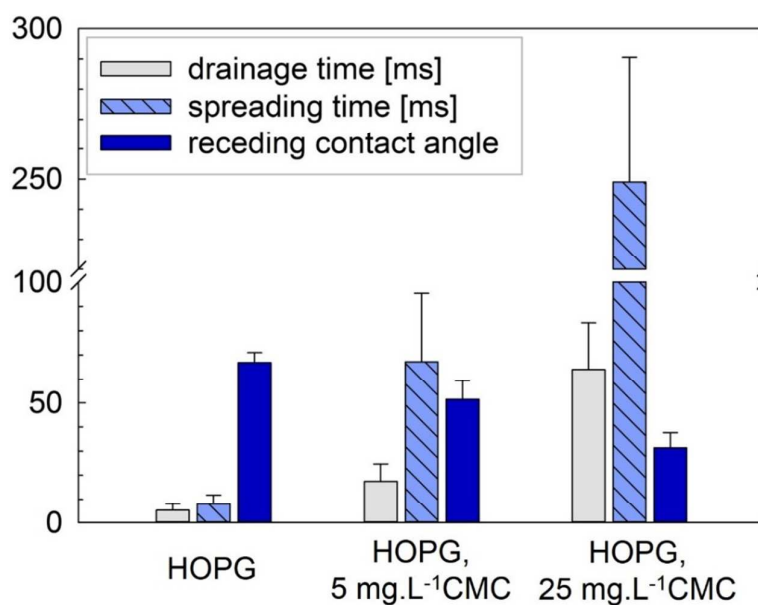


Figure 8. Comparison of average values of drainage time, spreading time, and static receding contact angle for bare HOPG, HOPG modified with 5 mg·L⁻¹, and HOPG modified with 25 mg·L⁻¹ of CMC.

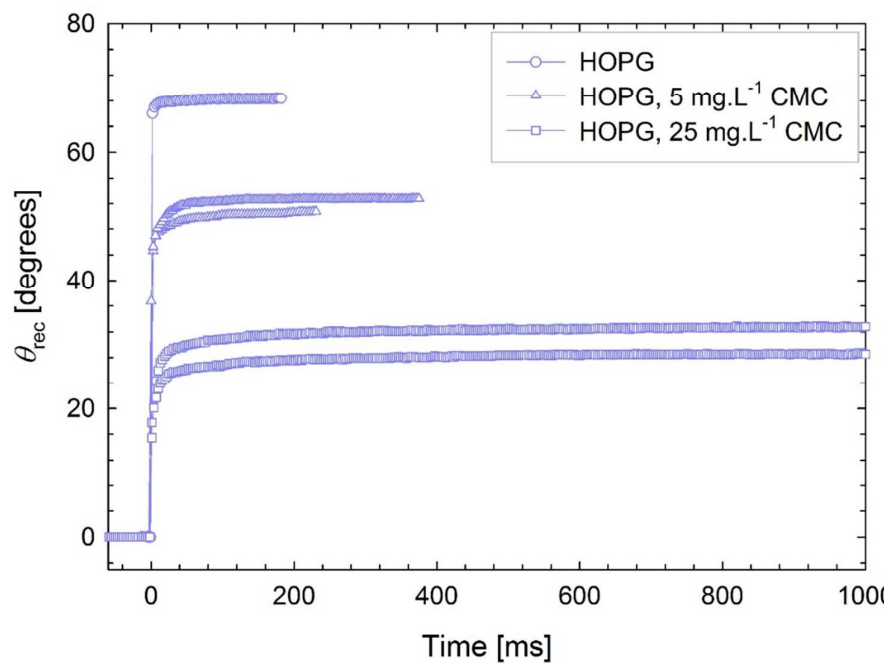


Figure 9. Dynamic receding contact angle as a function of time for bare HOPG (open circles), HOPG modified with 5 mg·L⁻¹ (open triangles), and HOPG modified with 25 mg·L⁻¹ (open squares). The experiments were carried out in 0.001 M KCl at pH 9.

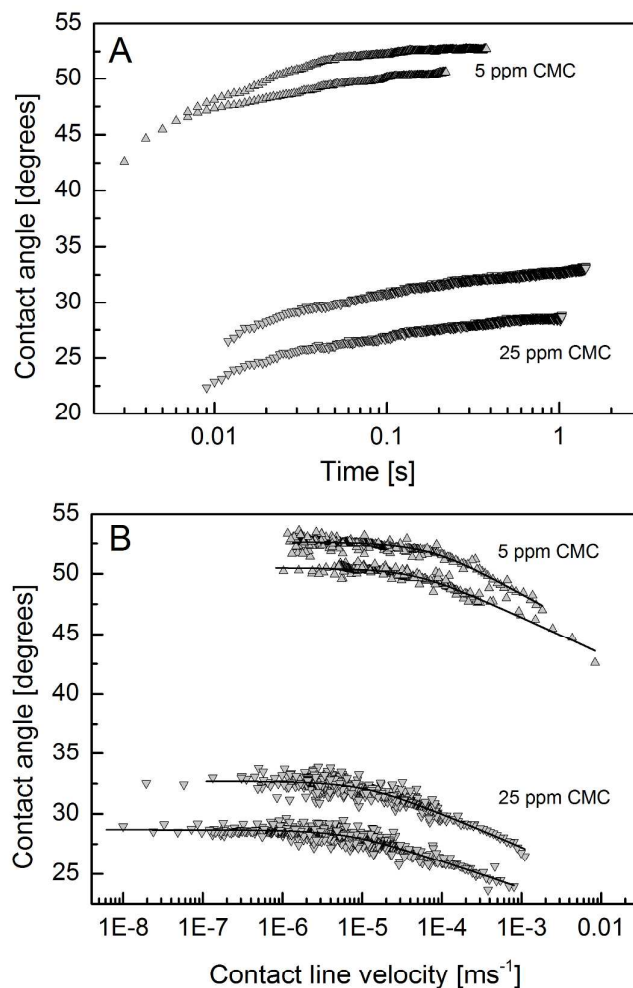


Figure 10. A: dynamic receding contact angle versus time for graphite modified with CMC (two datasets for each polymer concentration). B: Dynamic receding contact angle versus contact line velocity for graphite modified with CMC. $5 \text{ mg}\cdot\text{L}^{-1}$ CMC (upward-pointing triangles); $25 \text{ mg}\cdot\text{L}^{-1}$ CMC (downward-pointing triangles). The solid lines show the MKT fits to the experimental data.

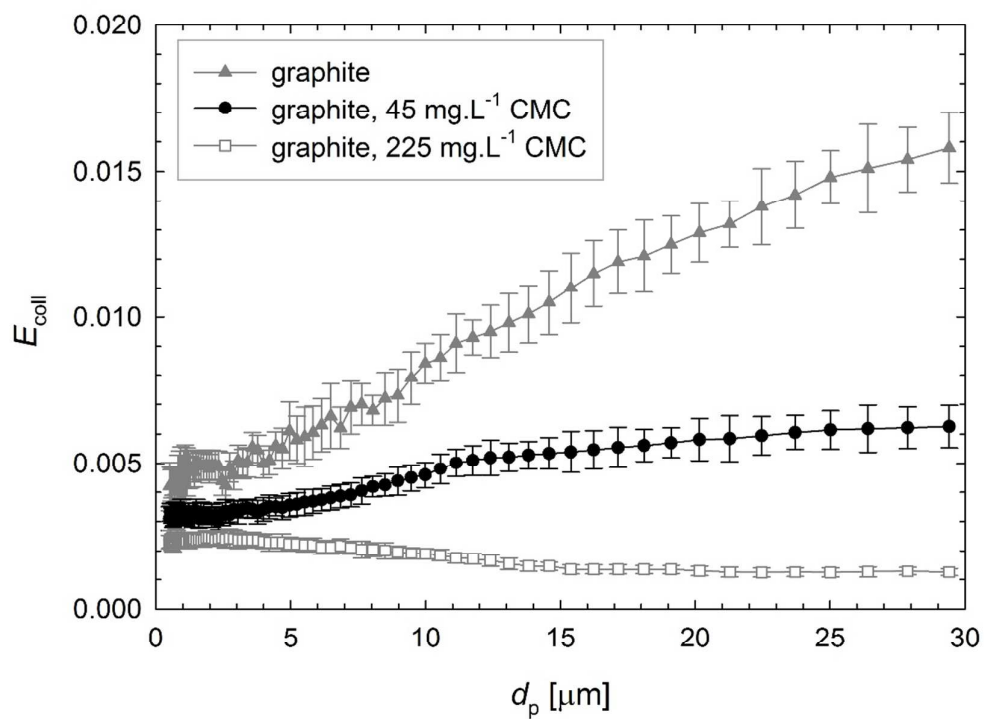


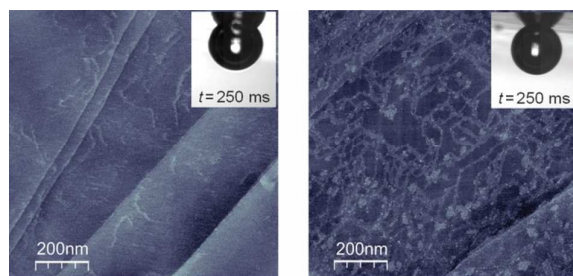
Figure 11. Particle-bubble collection efficiencies as a function of particle diameter for $d_{b(\text{average})} \sim 430 \mu\text{m}$ diameter bubbles in 0.001 M KCl, pH 9.

REFERENCES

1. M. Krasowska, S. L. Carnie, D. Fornasiero and J. Ralston, *Journal of Physical Chemistry C*, 2011, **115**, 11065-11076.
2. M. Krasowska, M. N. Popescu and J. Ralston, *Journal of Physics: Conference Series*, 2012, **392**.
3. L. Parkinson and J. Ralston, *Advances in Colloid and Interface Science*, 2011, **168**, 198-209.
4. R. Fetzer and J. Ralston, *Journal of Physical Chemistry C*, 2009, **113**, 8888-8894.
5. M. Krasowska, R. Krastev, M. Rogalski and K. Malysa, *Langmuir*, 2007, **23**, 549-557.
6. M. Krasowska and K. Malysa, *Advances in Colloid and Interface Science*, 2007, **134-135**, 138-150.
7. M. Krasowska, J. Zawala and K. Malysa, *Advances in Colloid and Interface Science*, 2009, **147-148**, 155-169.
8. A. H. Englert, M. Krasowska, D. Fornasiero, J. Ralston and J. Rubio, *International Journal of Mineral Processing*, 2009, **92**, 121-127.
9. R. F. Tabor, C. Wu, H. Lockie, R. Manica, D. Y. C. Chan, F. Grieser and R. R. Dagastine, *Soft Matter*, 2011, **7**, 8977-8983.
10. R. F. Tabor, F. Grieser, R. R. Dagastine and D. Y. C. Chan, *J. Colloid Interface Sci.*, 2012, **371**, 1-14.
11. B. A. Wills and T. Napier-Munn, in *Wills' mineral processing technology: an introduction to the practical aspects of ore treatment and mineral recovery*, Elsevier, London, 7th edn., 2006.
12. A. V. Nguyen, J. Ralston and H. J. Schulze, *International Journal of Mineral Processing*, 1998, **53**, 225-249.
13. A. V. Nguyen, H. J. Schulze and J. Ralston, *International Journal of Mineral Processing*, 1997, **51**, 183-195.
14. B. Albijanic, O. Ozdemir, A. V. Nguyen and D. Bradshaw, *Advances in Colloid and Interface Science*, 2010, **159**, 1-21.
15. A. V. Nguyen and H. Stechemesser, *Physical Chemistry Chemical Physics*, 2004, **6**, 429-433.
16. B. Albijanic, D. J. Bradshaw and A. V. Nguyen, *Minerals Engineering*, 2012, **36-38**, 309-313.
17. S. M. Bulatovic, *Handbook of flotation reagents: chemistry, theory and practice*, Elsevier, Boston, 2007.
18. T. N. Khmeleva, D. A. Beattie, T. V. Georgiev and W. M. Skinner, *Minerals Engineering*, 2003, **16**, 601-608.
19. T. N. Khmeleva, W. Skinner and D. A. Beattie, *International Journal of Mineral Processing*, 2005, **76**, 43-53.
20. R. J. Pugh, *International Journal of Mineral Processing*, 1989, **25**, 131-146.
21. R. J. Pugh, *International Journal of Mineral Processing*, 1989, **25**, 101-130.
22. A. Beaussart, L. Parkinson, A. Mierczynska-Vasilev and D. A. Beattie, *Journal of Colloid and Interface Science*, 2012, **368**, 608-615.
23. A. Beaussart, L. Parkinson, A. Mierczynska-Vasilev, J. Ralston and D. A. Beattie, *Langmuir*, 2009, **25**, 13290-13294.
24. M. Kor, P. M. Korczyk, J. Addai-Mensah, M. Krasowska and D. A. Beattie, *Langmuir*, 2014, **30**, 11975-11984.

25. I. G. Sedeva, R. Fetzer, D. Fornasiero, J. Ralston and D. A. Beattie, *Journal of Colloid and Interface Science*, 2010, **345**, 417-426.
26. J. Drzymala, *Advances in Colloid and Interface Science*, 1994, **50**, 143-185.
27. T. Wakamatsu and Y. Numata, *Minerals Engineering*, 1991, **4**, 975-982.
28. S. Gredelj, M. Zanin and S. R. Grano, *Minerals Engineering*, 2009, **22**, 279-288.
29. B. L. Pyke, R. F. Johnston and P. Brooks, *Minerals Engineering*, 1999, **12**, 851-862.
30. P. M. Afenya, *International Journal of Mineral Processing*, 1982, **9**, 303-319.
31. O. Bicak, Z. Ekmekci, D. J. Bradshaw and P. J. Harris, *Minerals Engineering*, 2007, **20**, 996-1002.
32. E. Burdukova, G. C. Van Leerdam, F. E. Prins, R. G. Smeink, D. J. Bradshaw and J. S. Laskowski, *Minerals Engineering*, 2008, **21**, 1020-1025.
33. L. T. Cuba-Chiem, L. Huynh, J. Ralston and D. A. Beattie, *Langmuir*, 2008, **24**, 8036-8044.
34. M. Khraisheh, C. Holland, C. Creany, P. Harris and L. Parolis, *International Journal of Mineral Processing*, 2005, **75**, 197-206.
35. S. Brunauer, P. H. Emmett and E. Teller, *J. Am. Chem. Soc.*, 1938, **60**, 309-319.
36. I. G. Sedeva, D. Fornasiero, J. Ralston and D. A. Beattie, *Langmuir*, 2010, **26**, 15865-15874.
37. M. Krasowska, A. Niecikowska and D. A. Beattie, *Surf. Innov.*, 2014, **2**, 151-159.
38. I. Horcas, R. Fernandez, J. M. Gomez-Rodriguez, J. Colchero, J. Gomez-Herrero and A. M. Baro, *Rev. Sci. Instr.*, 2007, **78**, 013705.
39. M. H. Rogers and G. N. Lance, *J. Fluid Mech.*, 1960, **7**, 617-631.
40. P. J. Sides and D. C. Prieve, *Langmuir* 2013, **29**, 13427-13432.
41. P. J. Sides, J. Newman, J. D. Hoggard and D. C. Prieve, *Langmuir*, 2006, **22**, 9765-9769.
42. T. Miettinen, PhD, University of South Australia, 2007.
43. J. Masliyah, R. Jauhari and M. Gray, *J. Chem. Eng. Sci.*, 1994, **49**, 1905-1911.
44. E. Klaseboer, R. Manica, D. Y. C. Chan and B. C. Khoo, *Eng. Anal. Bound. Elem.*, 2011, **35**, 489-494.
45. K. Malysa, M. Krasowska and M. Krzan, *Adv. Colloid Interface Sci.*, 2005, **114-115**, 205- 225.
46. T. D. Blake and J. M. Haynes, *J. Colloid Interface Sci.*, 1969, **30**, 421-423.
47. S. Glasstone, K. J. Laidler and H. Eyring, *The theory of rate processes: the kinetics of chemical reactions, viscosity, diffusion and electrochemical phenomena*, McGraw-Hill Book Company, Incorporated, 1941.
48. D. Seveno, A. Vaillant, R. Rioboo, H. Adão, J. Conti and J. De Coninck, *Langmuir*, 2009, **25**, 13034-13044.
49. S. Goossens, D. Seveno, R. Rioboo, A. Vaillant, J. Conti and J. De Coninck, *Langmuir*, 2011, **27**, 9866-9872.
50. L. Jiang, M. Krasowska, D. Fornasiero, P. Koh and J. Ralston, *Phys. Chem. Chem. Phys.*, 2010, **12**, 14527-14533.
51. Z. Dai, S. Dukhin, D. Fornasiero and J. Ralston, *J. Colloid Interface Sci.*, 2000, **197**, 275-292.
52. T. Ueno, S. Yokota, T. Kitaoka and H. Wariishi, *Carbohydrate Research*, 2007, **342**, 954-960.
53. J. F. Matthews, C. E. Skopec, P. E. Mason, P. Zuccato, R. W. Torget, J. Sugiyama, M. E. Himmelc and J. W. Brady, *Carbohydrate Research*, 2006, **341**, 138-152.
54. K. G. Marinova, R. G. Alargova, N. D. Denkov, O. D. Velev, D. N. Petsev, I. B. Ivanov and R. P. Borwankar, *Langmuir*, 1996, **12**, 2045-2051.

55. P. Creux, J. Lachaise, A. Graciaa, J. K. Beattie and A. M. Djerdjev, *Journal of Physical Chemistry B*, 2009, **113**, 14146-14150.
56. A. Quinn, R. Sedev and J. Ralston, *Journal of Physical Chemistry B*, 2003, **107**, 1163-1169.
57. O. Reynolds, *Philos. Trans. R. Soc. London*, 1886, **177**, 157-233.
58. A. Scheludko, *Adv. Colloid Interface Sci.*, 1967, **1**, 391-464.
59. D. Platikanov, *J. Phys. Chem.*, 1964, **68**, 3619-3624.
60. B. Jachimska, P. Warszynski and K. Malysa, *Colloids Surf., A*, 1998, **143**, 429-440.
61. A. Niccikowska, M. Krasowska, J. Ralston and K. Malysa, *J. Phys. Chem. C*, 2012, **116**, 3071-3078.
62. E. Bonaccorso, M. Kappl and H.-J. Butt, *Phys. Rev. Lett.*, 2002, **88**, 76103.
63. O. I. Vinogradova, *Int. J. Miner. Process.*, 1999, **56**, 31-60.
64. E. Lauga and M. P. Brenner, *Phys. Rev. E*, 2004, **70** 26311.
65. J. N. Israelachvili, *Intermolecular and Surface Forces*, Elsevier Science Publishing Co Inc, San Diego, 2011.
66. B. C. Donose, E. Taran, M. A. Hampton, S. I. Karakashev and A. V. Nguyen, *Adv. Powder Technol.*, 2009, **20**, 257-261.
67. C. Yang, T. Dabros, D. Li, J. Czarnecki and J. H. Masliyah, *J. Colloid Interface Sci.*, 2001, **243**, 128-135.
68. S. T. Lou, Z. Q. Ouyang, Y. Zhang, X. J. Li, J. Hu and M. Q. Li, *J. Vac. Sci. Technol. B*, 2000, **18**, 2573-2575.
69. H. Ana, G. Liub and V. S. J. Craig, *Adv. Colloid Interface Sci.*, 2014, **DOI: 10.1016/j.cis.2014.07.008**.
70. C. Duez, C. Ybert, C. Clanet and L. Bocquet, *Nature Physics* 2007, **3**, 180-183.
71. X. H. Zhang, A. Quinn and W. A. Ducker, *Langmuir*, 2008, **24**, 4756-4764.
72. X. H. Zhang, N. Maeda and V. S. J. Craig, *Langmuir*, 2006, **22**, 5025-5035.
73. R. Fetzer and J. Ralston, *Journal of Physical Chemistry C*, 2010, **114**, 12675-12680.
74. T. D. Blake and J. De Coninck, *Adv. Colloid Interface Sci.*, 2002, **96**, 21-36.
75. M. Ramiasa, J. Ralston, R. Fetzer and R. Sedev, *Advances in Colloid and Interface Science*, 2014, **206**, 275-293.
76. T. P. Coultate, *Food: The Chemistry of its Components*, Royal Society of Chemistry, Cambridge, 1996.



Bubble rise and collision against a graphite surface pre-treated with an adsorbed layer of carboxymethylcellulose. The adsorbed layer can prolong wetting film rupture, dramatically slow the dewetting of the mineral surface, and reduce the final contact angle of the bubble. Adsorption of CMC from a solution of higher polymer concentration amplifies the effect of the polymer.